



Article

Fluorine Atoms on C₆H₅-Corrole Affect the Interaction with M^{Pro} and PL^{Pro} Proteases of SARS-CoV-2: Molecular Docking and 2D-QSAR Approaches

Otávio Augusto Chaves ^{1,2,*} , Cláudio Eduardo Rodrigues-Santos ³, Áurea Echevarria ³,
Carolina Q. Sacramento ^{1,2} , Natalia Fintelman-Rodrigues ^{1,2} , Jairo R. Temerozo ^{4,5} ,
Hugo Caire Castro-Faria-Neto ¹ and Thiago Moreno Lopes e Souza ^{1,2,*}

- ¹ Laboratory of Immunopharmacology, Oswaldo Cruz Institute, Oswaldo Cruz Foundation (Fiocruz), Rio de Janeiro 21040-360, RJ, Brazil
 - ² Center for Technological Development in Health (CDTS), National Institute for Science and Technology on Innovation on Neglected Diseases Neglected Populations (INCT/IDNP), Oswaldo Cruz Foundation (Fiocruz), Rio de Janeiro 21040-360, RJ, Brazil
 - ³ Department of Organic Chemistry, Institute of Chemistry, Federal Rural University of Rio de Janeiro (UFRRJ), Seropédica 23890-000, RJ, Brazil
 - ⁴ Laboratory on Thymus Research, Oswaldo Cruz Institute, Oswaldo Cruz Foundation (Fiocruz), Rio de Janeiro 21040-360, RJ, Brazil
 - ⁵ National Institute for Science and Technology on Neuroimmunomodulation (INCT/NIM), Oswaldo Cruz Institute, Oswaldo Cruz Foundation (Fiocruz), Rio de Janeiro 21040-360, RJ, Brazil
- * Correspondence: otavioaugustochaves@gmail.com (O.A.C.); tmoreno@ccts.fiocruz.br (T.M.L.e.S.)



Citation: Chaves, O.A.;

Rodrigues-Santos, C.E.; Echevarria, Á.; Sacramento, C.Q.; Fintelman-Rodrigues, N.; Temerozo, J.R.; Castro-Faria-Neto, H.C.; Souza, T.M.L.e. Fluorine Atoms on C₆H₅-Corrole Affect the Interaction with M^{Pro} and PL^{Pro} Proteases of SARS-CoV-2: Molecular Docking and 2D-QSAR Approaches. *Int. J. Mol. Sci.* **2022**, *23*, 10936. <https://doi.org/10.3390/ijms231810936>

Academic Editors: Vitaliy Borisov and Jia-Zhong Li

Received: 16 August 2022

Accepted: 13 September 2022

Published: 19 September 2022

Publisher's Note: MDPI stays neutral with regard to jurisdictional claims in published maps and institutional affiliations.



Copyright: © 2022 by the authors. Licensee MDPI, Basel, Switzerland. This article is an open access article distributed under the terms and conditions of the Creative Commons Attribution (CC BY) license (<https://creativecommons.org/licenses/by/4.0/>).

Abstract: The chymotrypsin-like cysteine protease (3CL^{Pro}, also known as main protease—M^{Pro}) and papain-like protease (PL^{Pro}) of severe acute respiratory syndrome coronavirus 2 (SARS-CoV-2) have been used as the main targets for screening potential synthetic inhibitors for posterior in vitro evaluation of the most promising compounds. In this sense, the present work reports for the first time the evaluation of the interaction between M^{Pro}/PL^{Pro} with a series of 17 porphyrin analogues-corrole (C1), *meso*-aryl-corrole (C2), and 15 fluorinated-*meso*-aryl-corrole derivatives (C3–C17) via molecular docking calculations. The impact of fluorine atoms on *meso*-aryl-corrole structure was also evaluated in terms of binding affinity and physical-chemical properties by two-dimensional quantitative structure–activity relationship (2D-QSAR). The presence of phenyl moieties increased the binding capacity of corrole for both proteases and depending on the position of fluorine atoms might impact positively or negatively the binding capacity. For M^{Pro} the *para*-fluorine atoms might decrease drastically the binding capacity, while for PL^{Pro} there was a certain increase in the binding affinity of fluorinated-corroles with the increase of fluorine atoms into *meso*-aryl-corrole structure mainly from tri-fluorinated insertions. The 2D-QSAR models indicated two separated regions of higher and lower affinity for M^{Pro}:C1–C17 based on dual electronic parameters (σ_I and σ_R), as well as one model was obtained with a correlation between the docking score value of M^{Pro}:C2–C17 and the corresponding ¹³C nuclear magnetic resonance (NMR) chemical shifts of the sp² carbon atoms (δ_{C-1} and δ_{C-2}) of C2–C17. Overall, the fluorinated-*meso*-aryl-corrole derivatives showed favorable in silico parameters as potential synthetic compounds for future in vitro assays on the inhibition of SARS-CoV-2 replication.

Keywords: corroles; SARS-CoV-2; M^{Pro}; PL^{Pro}; molecular docking; 2D-QSAR

1. Introduction

The severe acute respiratory syndrome coronavirus 2 (SARS-CoV-2) was discovered in China (December/2019) and quickly spread globally, being classified by the World Health Organization (WHO) as a pandemic in February 2020 [1]. Since SARS-CoV-2 was discovered until the time of writing (end of August 2022), there have been over 601 million

confirmed cases and 6.49 million deaths worldwide [2], overtaking both SARS-CoV and Middle East respiratory syndrome (MERS) in 2003 and 2012, respectively [3]. SARS-CoV-2 is still circulating mainly due to the variants of concern (VoC) that might escape the immune response induced by vaccines [4–7] and the few approved drugs by the U.S. Food and Drug Administration (FDA), e.g., remdesivir and baricitinib [8,9] reinforces the continuous necessity of drug development against 2019 coronavirus disease (COVID-19).

Different authors have evaluated the capacity of commercial drugs, natural products, and novel drugs to inhibit the SARS-CoV-2 proteases [10–15]. Basically, the coronaviruses have a long ribonucleic acid (RNA) strand which is used to synthesize two long polyproteins in the infected cells. The main products of these polyproteins include both structural and non-structural proteins that are responsible for the formation of new virions, and two proteases: chymotrypsin-like cysteine protease (3CL^{pro}, also known as main protease-M^{pro}) and papain-like protease (PL^{pro}) [11,16–19]. The proteases cleavage the polyproteins into functional pieces, as example M^{pro} targets 7 and 11 cleavage sites into open reading frame (ORF) 1a and 1b, respectively, while PL^{pro} is responsible for producing non-structural protein nsp1, nsp2, and nsp3 [20,21]. The importance of M^{pro} as a target has been reinforced by the drug PF-07321332 (PAXLOVIDTM; Pfizer), which reduced COVID-19-associated hospitalization by 80% [22,23].

Cyclic organic compounds that are based on four pyrrole moieties with three connections by methine group and only one direct pyrrole-pyrrole bond (lacking a methine group) with an extra NH proton are known as corroles (porphyrin analogues) [24]. These compounds show interesting photophysical and photochemical properties, including low aggregation tendency, strong absorption at high wavelengths, large Stokes shift, and high fluorescent quantum yield [25–27]. For this reason, corroles are evaluated in terms of applications in photodynamic therapy (PDT) [28], antimicrobial photodynamic therapy (aPDT) [29,30], theranostic agent [31,32], and biomacromolecules site markers [24]. Despite the fact that porphyrins have already been evaluated as potential candidates to inhibit the interaction between SARS-CoV-2 and human angiotensin-converting enzyme 2 (ACE2) [33,34], as well as photosensitizer to photodynamically destroy the SARS-CoV-2 structure [35,36], there are not any reports on the capacity of corroles to inhibit SARS-CoV-2 replication or the virus proteases.

The fluorine atom insertion into small organic compounds have been widely used in pharmacology to increase the biological properties, as an example enhance a number of pharmacokinetic and physicochemical properties such as metabolic stability, membrane permeation, and binding affinity to target proteins [37–39]. In the case of corroles, it has been reported that the presence of fluorine atoms may enrich the photostability, singlet oxygen production, lipophilicity, selective accumulation in tumor cells, protein binding, and catalytic antioxidants for the attenuation of diabetes mellitus [24,30].

Thus, based on the high necessity of screening potential SARS-CoV-2 inhibitors, as well as the importance of corroles in the pharmacology and the positive effect of fluorine atom insertion to increase the pharmacokinetic and physicochemical properties, the present work reports the interaction between M^{pro}/PL^{pro} from SARS-CoV-2 with corrole (C1, Figure 1), *meso*-aryl-corrole (C₆H₅-corrole, C2, Figure 1), and 15 fluorinated-*meso*-aryl-corrole derivatives (C3–C17, Figure 1) via molecular docking calculations. The impact of fluorine atoms on *meso*-aryl-corrole structure was also evaluated in terms of binding affinity and physical-chemical properties by two-dimensional quantitative structure–activity relationship (2D-QSAR). To the best of our knowledge, this is the first *in silico* report that explores the potential inhibitory effects of corroles against both M^{pro} and PL^{pro} proteases.

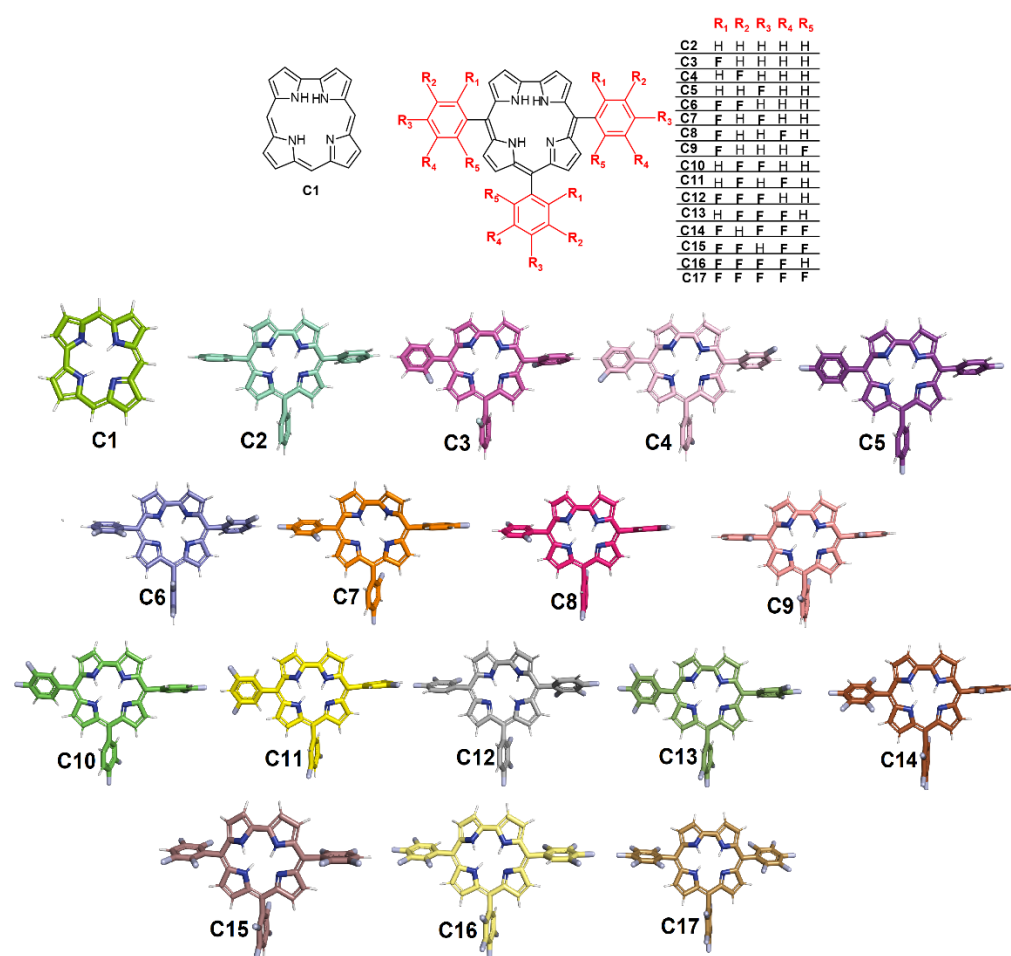


Figure 1. The chemical structures of corrole **C1**, *meso*-aryl-corrole (**C2**), and fluorinated-*meso*-aryl-corrole derivatives (**C3**–**C17**). The color used to represent the 3D structures of the corroles corresponding to the same used in the docking representations.

2. Results

2.1. Molecular Docking Evaluation for M^{Pro} Enzyme

The Gold 2020.2 software (Cambridge Crystallographic Data Center Software Ltd., Cambridge, UK) generated at least 10 different poses for each corrole derivative and the pose with the largest binding affinity (corresponding to the highest positive score value and more buried into the protein cavity) was considered the best pose and analyzed in terms of interaction. Table 1 summarizes the largest docking score value for all corrole derivatives, e.g., for M^{Pro} the highest score was obtained to **C2** (*meso*-aryl-corrole) than for **C1** (corrole): 35.68 and 25.76 dimensionless, respectively. The insertion of fluorine atoms into the phenyl moiety directly impacted the binding capacity of C₆H₅-corrole as revealed by the increase in the docking score value. Additionally, the docking score for the fluorinated-corroles **C3**–**C17** (Table 1) suggested that the position of the fluorine atoms drastically impacted the score. As an example, the docking score value for the mono-substituted-fluorinated-corroles **C3**–**C5** decreased drastically for fluorine atoms in the *para* position: 35.98, 36.44, and 24.65 dimensionless for M^{Pro}:**C3**/**C4**/**C5**, respectively.

Table 1. The highest molecular docking score value (dimensionless) for the interaction between M^{Pro}/PL^{Pro} and each corrole under study (C1–C17).

Compound	M ^{Pro}	PL ^{Pro}
C1	25.76	25.25
C2	35.68	32.44
C3	35.98	30.41
C4	36.44	31.76
C5	24.65	30.38
C6	34.98	31.29
C7	22.43	30.13
C8	36.24	31.99
C9	34.50	31.84
C10	24.92	34.69
C11	35.64	32.39
C12	25.47	31.18
C13	26.37	40.65
C14	21.76	37.95
C15	36.57	35.07
C16	24.81	38.97
C17	22.84	39.29

Figure 2A depicts the M^{Pro} enzyme and the catalytic dyad that is composed by His-41 and Cys-145 residues with the presence of a key water molecule that is important for the catalysis. Figure 2B–G show the superposition of the best docking pose for the interaction between M^{Pro} with the corresponding non- (C1, C2) mono- (C3–C5), di- (C6–C11), tri- (C12, C13), tetra- (C14–C16), and penta- (C17) fluorinated-corroles. According to the surface representation of the M^{Pro} structure, all the compounds under study are buried into the catalytic pocket assuming different binding profiles depending on the fluorinated position in C₆H₅-corrole structure. Table 2 summarizes the amino acid residues with the corresponding intermolecular force and distance that is involved in the interaction process M^{Pro}:C1–C17. In this case, van der Waals interactions was suggested as the main intermolecular force and hydrogen bonding was also detected, except for C2. Figure 3 depicts the 3D interaction of each corrole in the M^{Pro} catalytic site, highlighting the key amino acid residues that might interact with each compound.

2.2. Molecular Docking Evaluation for PL^{Pro} Enzyme

For the other SARS-CoV-2 protease, known as PL^{Pro}, Table 1 also summarizes the largest docking score value for all corrole derivatives, suggesting a higher score value for C2 (*meso*-aryl-corrole) than C1 (corrole) with values of 32.44 and 25.25 dimensionless, respectively. The insertion of fluorine atoms in the phenyl moiety also directly impacted the binding capacity of C₆H₅-corrole to PL^{Pro} as revealed by the increase in the docking score value. However, differently from M^{Pro}, the fluorine position in C3–C17 did not show any specific trend (Table 1); as an example, the docking score value for the mono-substituted-fluorinated-corroles C3–C5 are quite similar: 30.41, 31.76, and 30.38 dimensionless for C3, C4, and C5, respectively. Nevertheless, a certain increase was noticed in the binding affinity of fluorinated-corroles to PL^{Pro} with the increase of fluorine atoms in the *meso*-aryl-corrole structure, mainly from tri-fluorinated insertions, e.g., a docking score value for C13–C17 is higher than 35 dimensionless.

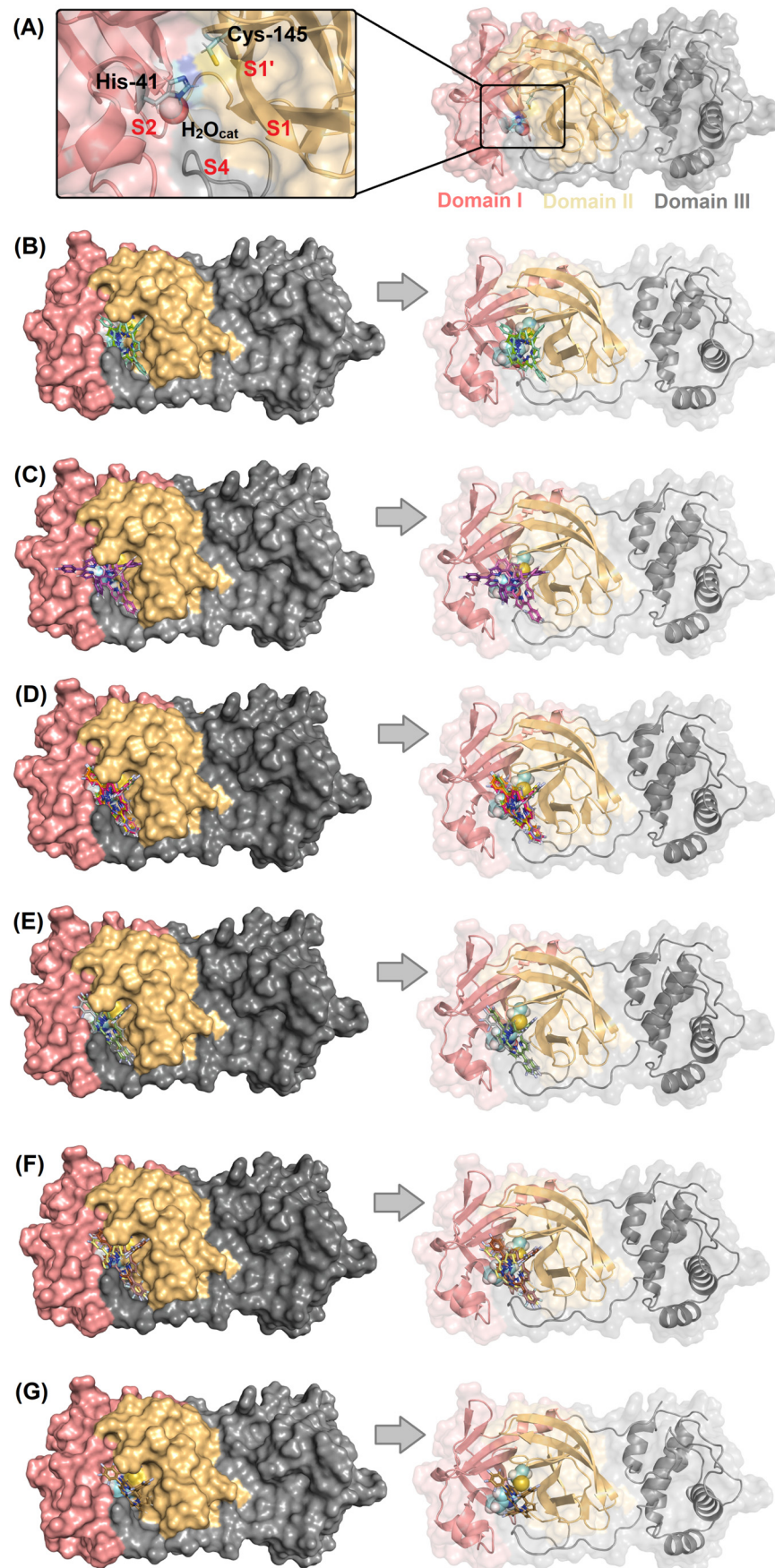


Figure 2. (A) The 3D structure for $MPTO$ (PDB code: 6LU7) highlighting the catalytic Cys-His dyad (as stick in cyan) and catalytic water (H_2O_{cat}) as a sphere. Superposition of the best docking pose for the

interaction between M^{Pro} (as surface) with (B) non-fluorinated-corroles (C1, C2), (C) mono-fluorinated-corroles (C3–C5), (D) di-fluorinated-corroles (C6–C11), (E) tri-fluorinated-corroles (C12, C13), (F) tetra-fluorinated-corroles (C14–C16), and (G) penta-fluorinated-corroles (C17). For better interpretation, only the monomer and not the dimer form of M^{Pro} was represented. The chemical structure and the corresponding carbon's color of each corrole that was used in this study are in stick representation according to the 3D chemical structure of the Figure 1. Elements' color: hydrogen, nitrogen, fluorine, and oxygen in white, dark blue, light blue, and red, respectively.

Table 2. Molecular docking results for the interaction between M^{Pro}:C1–C17.

Compound	Amino Acid Residue	Interaction Type	Distance (Å)
C1	Met-49	Van der Waals	1.70
	Asn-142	Van der Waals	2.90
	Cys-145	Hydrogen bonding	3.20
	Met-165	Van der Waals	3.20
	Gln-189	Van der Waals	3.60
C2	Leu-27	Van der Waals	2.90
	His-41	Van der Waals	3.00
	Met-49	Van der Waals	1.90
	Cys-145	Van der Waals	2.60
	Met-165	Van der Waals	2.30
	Pro-168	Van der Waals	3.00
C3, C4	Gln-189	Van der Waals	2.10
	Thr-25	Van der Waals	1.20
	Leu-27	Van der Waals	2.70
	His-41	Van der Waals	2.70
	Met-49	Van der Waals	2.40
	Cys-145	Van der Waals	3.00
	Met-165	Van der Waals	2.60
	Pro-168	Van der Waals	2.80
C5	Gln-1896	Hydrogen bonding	3.70
	Thr-24	Hydrogen bonding	2.10
	Thr-25	Van der Waals	1.50
	Met-49	Van der Waals	2.50
	Cys-145	Van der Waals	3.70
	His-163	Van der Waals	1.40
	Glu-166	Van der Waals	2.40
	His-172	Van der Waals	1.60
C6, C8, C9, C11	Gln-189	Van der Waals	2.40
	Thr-25	Van der Waals	2.60
	Leu-27	Van der Waals	1.80
	His-41	Van der Waals	2.70
	Met-49	Van der Waals	1.80
	Asn-142	Van der Waals	1.90
	Gly-143	Van der Waals	2.60
	Cys-145	Hydrogen bonding	2.20
	Met-165	Van der Waals	2.60
Leu-167	Van der Waals	2.70	
C7, C10	Gln-189	Hydrogen bonding	2.00
	Leu-27	Van der Waals	2.10
	His-41	Van der Waals	1.50
	Met-49	Van der Waals	1.70
	Asn-142	Van der Waals	3.70

Table 2. Cont.

Compound	Amino Acid Residue	Interaction Type	Distance (Å)
C12, C13	Leu-27	Van der Waals	2.20
	His-41	Van der Waals	2.40
	Met-49	Van der Waals	1.60
	Asn-142	Van der Waals	2.00
	Met-165	Van der Waals	1.20
	Leu-167	Van der Waals	2.80
	Gln-189	Hydrogen bonding	2.10
C14, C16	His-41	Van der Waals	3.10
	Met-49	Van der Waals	2.50
	Asn-142	Van der Waals	2.50
	Met-165	Van der Waals	1.10
	Glu-166	Van der Waals	3.40
	Gln-189	Hydrogen bonding	2.10
C15	Thr-25	Van der Waals	2.80
	His-41	Van der Waals	2.90
	Met-49	Van der Waals	2.30
	Asn-142	Van der Waals	3.70
	Cys-145	Hydrogen bonding	2.30
	Met-165	Van der Waals	2.70
	Leu-167	Van der Waals	2.20
Glu-189	Van der Waals	3.00	
C17	His-41	Van der Waals	2.40
	Met-49	Van der Waals	2.70
	Tyr-54	Van der Waals	1.70
	Asn-142	Van der Waals	2.40
	Met-165	Van der Waals	1.20
	Asp-187	Van der Waals	1.30
	Gln-189	Hydrogen bonding	2.00
	H ₂ O _{cat}	Van der Waals	2.50

Figure 4A depicts the PL^{PRO} structure and the catalytic triad that is composed by Cys-112, His-273, and Asp-287 residues without the necessity of specific internal water to occur the catalysis. Figure 4B–G show the superposition of the best docking pose for the interaction between PL^{PRO} with the corresponding non- (C1, C2) mono- (C3–C5), di- (C6–C11), tri- (C12, C13), tetra- (C14–C16), and penta- (C17) fluorinated-corroles. According to the surface representation of the protease structure, all the compounds can be buried between the catalytic pocket of chain A (in blue surface) and in part into the surface of not a catalytic pocket of chain C (in green surface) assuming a different binding profile. Curiously, for mono-fluorinated-corroles, even though the docking score value did not show a decrease in the binding affinity with fluorine at the *para* position (R₃), from Figure 4B there is an indication that C5 is not interacting preferentially in the catalytic site compared with C3 and C4. Table 3 summarizes the amino acid residues with the corresponding intermolecular forces and distance that is involved in the interaction process with the corrole derivatives indicating van der Waals interactions as the main intermolecular force that is responsible for the interaction between PL^{PRO}:C1–C17, however, hydrogen bonding was also detected, except for C1, C2, and C5. In addition, Figure 5 depicts the 3D interaction of each corrole into PL^{PRO} catalytic site highlighting the key amino acid residues that might interact with each compound.

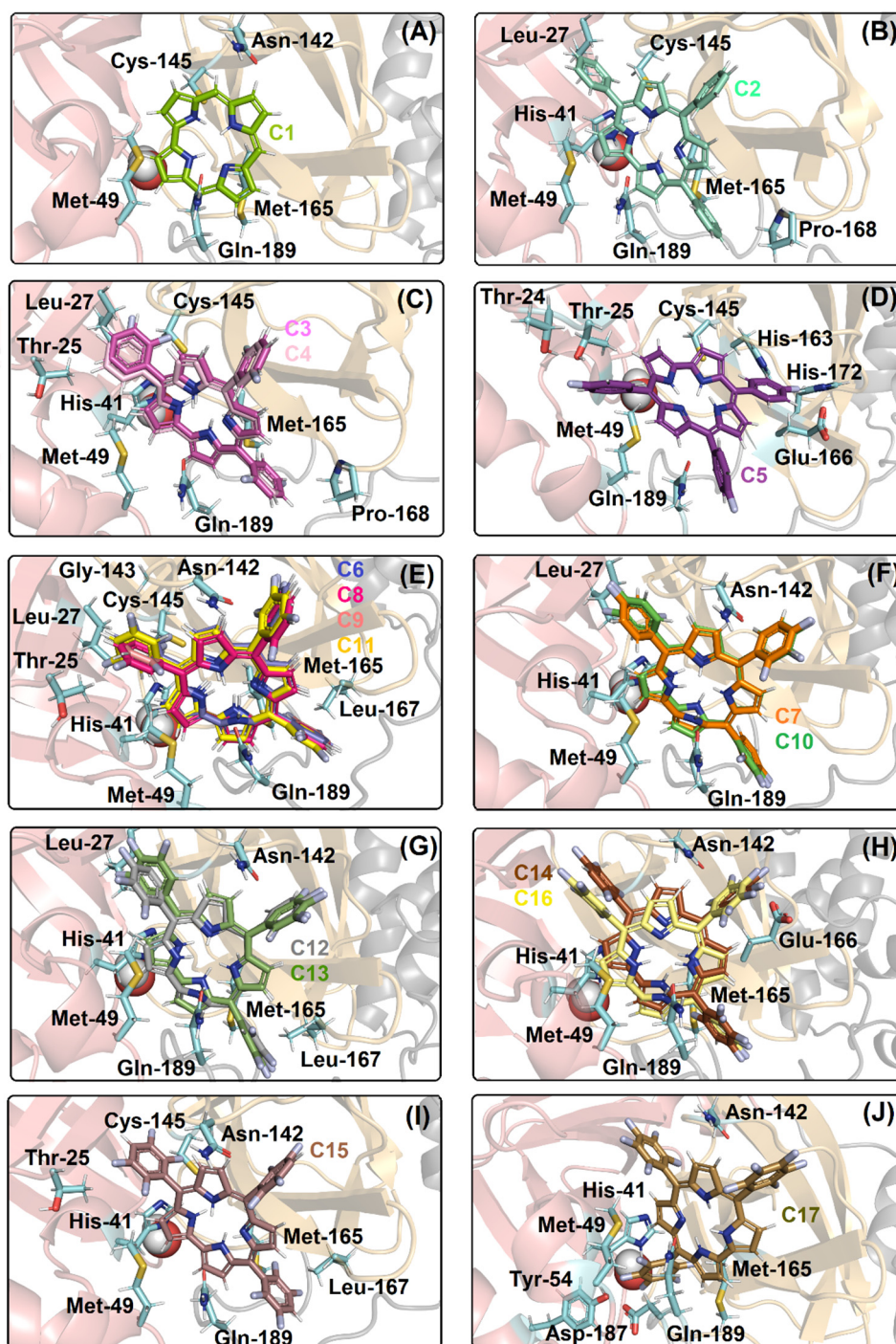


Figure 3. The best docking pose into the catalytic site of M^{PTO} for (A) C1; (B) C2, (C) C3, C4; (D) C5; (E) C6, C8, C9, C11; (F) C7, C10; (G) C12, C13; (H) C14, C16; (I) C15; and (J) C17. The H_2O_{cat} is represented as a sphere, while the selected amino acid residues that are interacting with the corrole structure are in stick representation in cyan. The M^{PTO} structure is in cartoon representation, being divided into domains I, II, and III in beige, light orange, and gray, respectively. The chemical structure and the corresponding carbon's color of each corrole that was used in this study are in stick representation according to the 3D chemical structure of the Figure 1. The elements' color: hydrogen, nitrogen, fluorine, and oxygen in white, dark blue, light blue, and red, respectively.

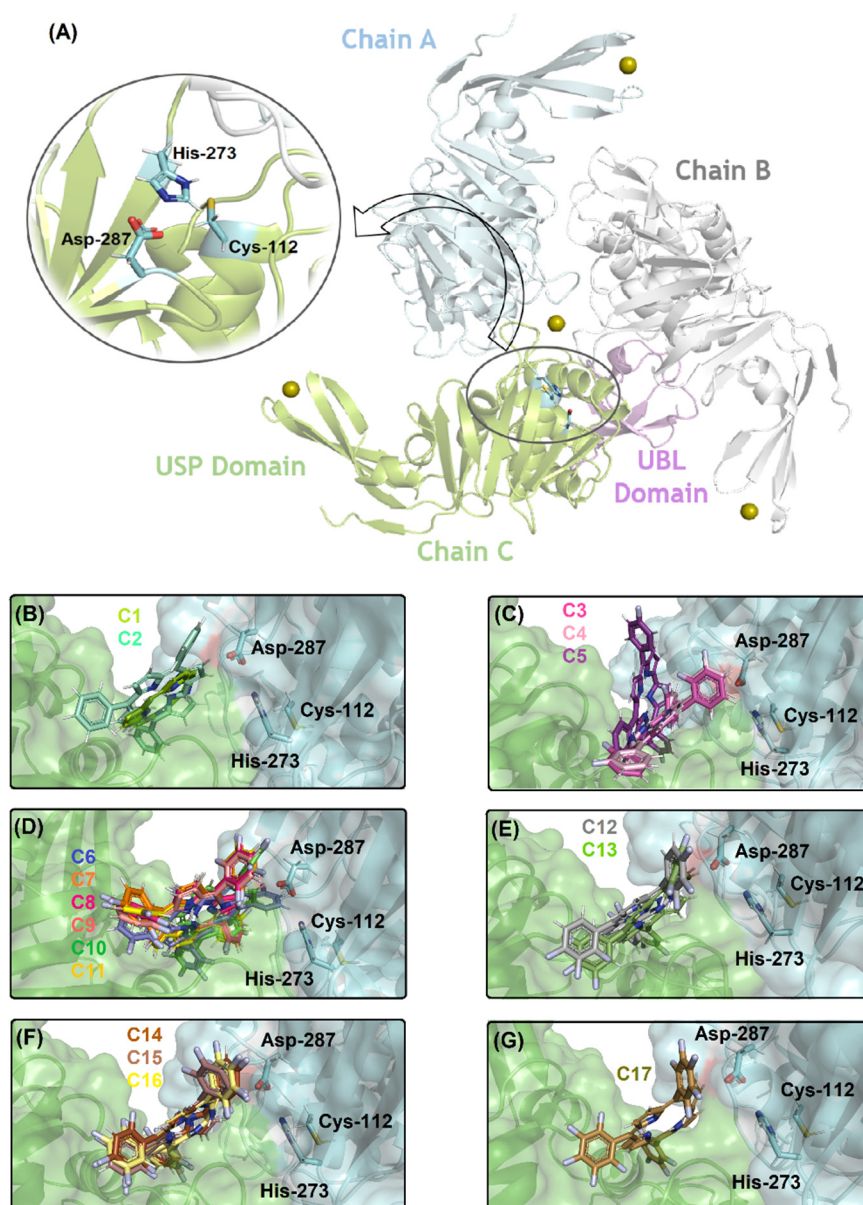


Figure 4. (A) The 3D structure for PL^{Pro} (PDB code: 6W9C) highlighting the catalytic Cys-His-Asp triad (as stick in cyan). Superposition of the best docking pose for the interaction between PL^{Pro} (as surface) with (B) non-fluorinated-corroles (C1, C2), (C) mono-fluorinated-corroles (C3–C5), (D) di-fluorinated-corroles (C6–C11), (E) tri-fluorinated-corroles (C12, C13), (F) tetra-fluorinated-corroles (C14–C16), and (G) penta-fluorinated-corroles (C17) into the catalytic triad pocket. The PL^{Pro} structure is in cartoon representation divided into chains A, B, and C in blue, light gray, and green, respectively. The *N*-terminal ubiquitin-like (UBL) and *C*-terminal ubiquitin-specific (USP) domains are in violet and green (the β -sheets which interact with Zn(II) ion) into chain C, respectively. The Zn(II) ions are in sphere representation in olive, and the corresponding carbon's color of each corrole that was used in this study is in stick representation according to the 3D chemical structure of the Figure 1. The elements' color: hydrogen, nitrogen, fluorine, and oxygen in white, dark blue, light blue, and red, respectively.

Table 3. Molecular docking results for the interaction between PL^{Pro}:C1–C17.

Compound	Amino Acid Residue/Chain	Interaction Type	Distance (Å)
C1	Lys-106/Chain A	Van der Waals	3.40
	Asp-287/Chain A	Van der Waals	3.10
	Leu-290/Chain A	Van der Waals	3.20
	Pro-249/Chain C	Van der Waals	1.80
	Asn-258/Chain C	Van der Waals	3.70
	Tyr-265/Chain C	Van der Waals	1.70
C2	Trp-107/Chain A	Van der Waals	1.80
	Asp-287/Chain A	Van der Waals	3.50
	Leu-290/Chain A	Van der Waals	0.60
	Pro-249/Chain C	Van der Waals	3.20
	Tyr-265/Chain C	Van der Waals	3.20
	Pro-300/Chain C	Van der Waals	1.80
C3, C4	Lys-106/Chain A	Van der Waals	3.00
	Trp-107/Chain A	Van der Waals	1.80
	Lys-278/Chain A	Van der Waals	2.00
	Asp-287/Chain A	Van der Waals	3.70
	Leu-290/Chain A	Van der Waals	3.20
	Pro-249/Chain C	Van der Waals	1.70
	Tyr-265/Chain C	Van der Waals	2.30
	Asn-268/Chain C	Hydrogen bonding	2.10
Tyr-269/Chain C	Van der Waals	3.50	
C5	Lys-106/Chain A	Van der Waals	3.10
	Trp-107/Chain A	Van der Waals	2.10
	Leu-290/Chain A	Van der Waals	2.60
	Leu-163/Chain C	Van der Waals	3.30
	Pro-249/Chain C	Van der Waals	2.50
	Tyr-265/Chain C	Van der Waals	3.00
C6	Trp-107/Chain A	Van der Waals	2.50
	Asp-287/Chain A	Van der Waals	2.90
	Leu-290/Chain A	Van der Waals	2.80
	Pro-249/Chain C	Van der Waals	1.70
	Tyr-265/Chain C	Van der Waals	2.90
	Asn-268/Chain C	Hydrogen bonding	2.90
	Tyr-269/Chain C	Van der Waals	2.20
	Pro-300/Chain C	Van der Waals	2.80
C7, C8, C9, C10, C11	Trp-107/Chain A	Van der Waals	3.70
	Lys-275/Chain A	Hydrogen bonding	1.10
	Asp-287/Chain A	Van der Waals	2.20
	Leu-290/Chain A	Van der Waals	1.20
	Pro-249/Chain C	Van der Waals	1.30
	Gln-251/Chain C	Hydrogen bonding	3.30
	Tyr-265/Chain C	Van der Waals	2.60
	Asn-268/Chain C	Hydrogen bonding	2.90
C12, C13	Trp-107/Chain A	Van der Waals	1.90
	Lys-275/Chain A	Hydrogen bonding	2.50
	Asp-287/Chain A	Van der Waals	3.10
	Leu-290/Chain A	Van der Waals	2.00
	Pro-249/Chain C	Van der Waals	1.70
	Tyr-265/Chain C	Van der Waals	3.20
	Asn-268/Chain C	Hydrogen bonding	3.30
	Pro-300/Chain C	Van der Waals	2.90
C14, C15, C16	Trp-107/Chain A	Van der Waals	1.90
	Lys-275/Chain A	Hydrogen bonding	1.70
	Asp-287/Chain A	Van der Waals	2.30
	Leu-290/Chain A	Van der Waals	1.40
	Pro-249/Chain C	Van der Waals	1.60
	Tyr-265/Chain C	Van der Waals	3.30
	Asn-268/Chain C	Hydrogen bonding	3.70
	Pro-300/Chain C	Van der Waals	3.40

Table 3. Cont.

Compound	Amino Acid Residue/Chain	Interaction Type	Distance (Å)
C17	Trp-107/Chain A	Van der Waals	3.10
	Lys-275/Chain A	Hydrogen bonding	2.60
	Asp-287/Chain A	Van der Waals	3.40
	Leu-290/Chain A	Van der Waals	1.20
	Asp-165/Chain C	Van der Waals	1.90
	Pro-249/Chain C	Van der Waals	1.50
	Tyr-265/Chain C	Van der Waals	2.90
	Asn-268/Chain C	Hydrogen bonding	3.70
	Pro-300/Chain C	Van der Waals	2.70

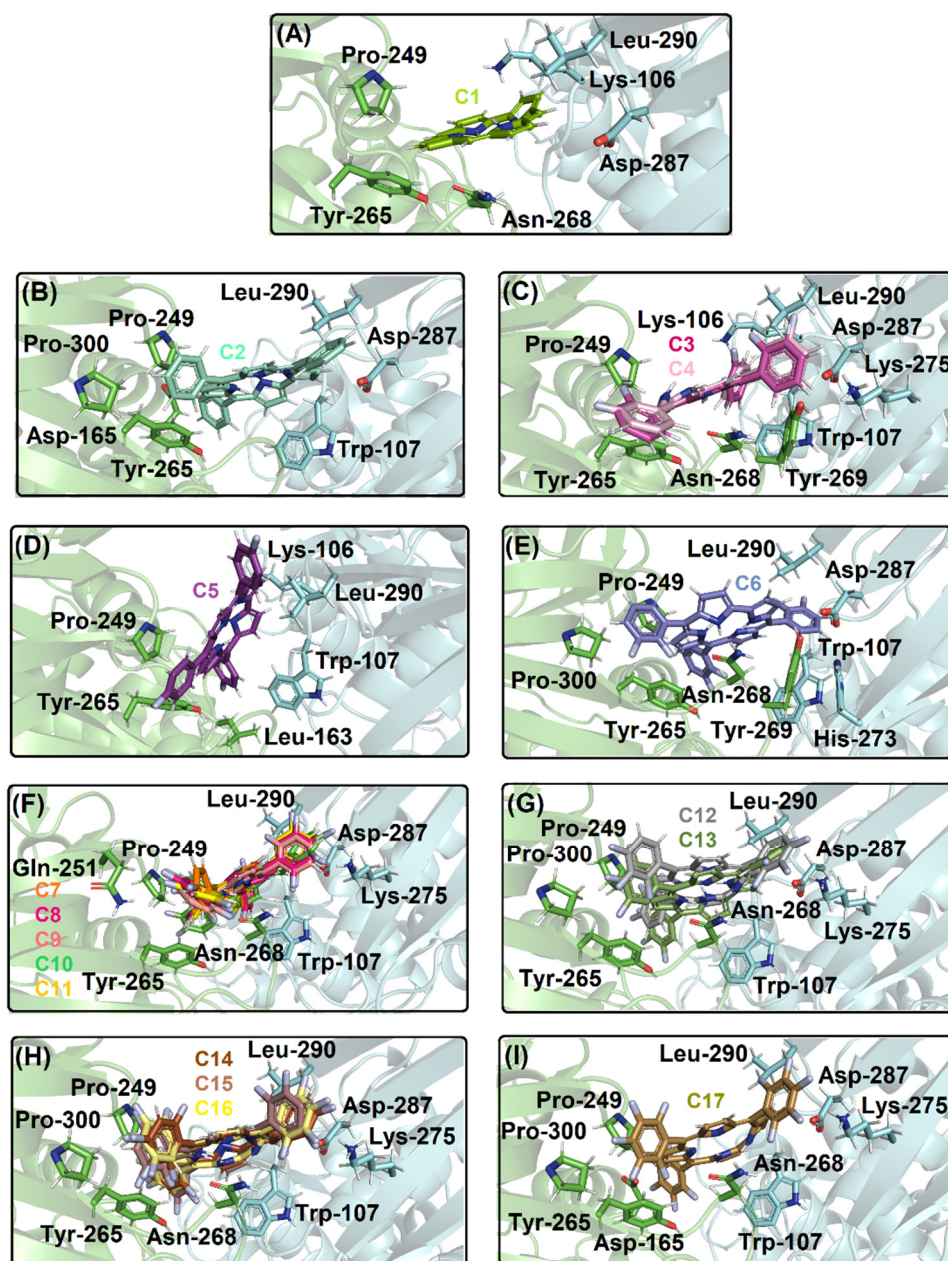


Figure 5. The best docking pose into the catalytic site of PL^{Pro} for (A) C1; (B) C2; (C) C3, C4; (D) C5; (E) C6; (F) C7, C8, C9, C10, C11; (G) C12, C13; (H) C14, C15, C16; and (I) C17. The PL^{Pro} structure is

in cartoon representation divided into chains A, B, and C in blue, light gray, and green, respectively. The selected amino acid residues into chain A and C are in stick representation in blue and green, respectively. The chemical structure and the corresponding carbon's color of each corrole that was used in this study is in stick representation according to the 3D chemical structure of the Figure 1. The elements' color: hydrogen, nitrogen, fluorine, and oxygen in white, dark blue, light blue, and red, respectively.

2.3. 2D Quantitative Structure–Activity Relationship (2D-QSAR) Model

In attempt to correlate the docking score values that were obtained for M^{Pro} and PL^{Pro} with the corroles C1–C17, initially these values were correlated with the electronic effects (Hammett constants, dual parameters, Swain–Lupton inductive, and resonance parameters) and lipophilic (logP) effects. A sigmoidal correlation between the docking score values for M^{Pro}:C1–C17 with dual electronic parameters (σ_I and σ_R) with $R^2 = 0.9953$ was observed. On the other hand, regarding the protease PL^{Pro}, a significant correlation with the investigated parameters was not observed.

Additionally, some molecular descriptors such as polarizability (POLZ), superficial tension (ST), molar volume (MV), molar refractivity (MR), and the ¹³C NMR chemical shifts of the sp² carbon atoms (δ_{C-1} and δ_{C-2}) adjacent to the fluorinated ring were calculated for each *meso*-aryl-corrole (C2–C17) from ACD/ChemSketch software [40] (Table 4). To understand the interaction among these compounds with M^{Pro} or PL^{Pro} proteases, several correlation equations were obtained by BuildQSAR 1.0 software (Universidade Federal do Espírito Santo, Vitória, Espírito Santo, Brazil) [41]. From the results that were obtained via molecular descriptors, there is the indication of only one model (M^{Pro} score value and ¹³C NMR chemical shifts of the sp² carbons atoms, δ_{C-1} and δ_{C-2} , adjacent to the fluorinated ring, Equation (1)) with robust statistics parameters that respect the quality of the adjustment of the data in the 2D-model: the correlation coefficient (r^2) and Fisher (F) for the statistical significance values of 0.96 and 301.92, respectively, and predictability through cross validation (q^2) and the standard deviation of cross validation (S_{PRESS}) values of 0.94 and 1.463, respectively [42,43].

$$\text{M}^{\text{Pro}} \text{ score} = 34.79 (\pm 4.32) \delta_{C-1} - 33,001.18 (\pm 4469.79) \quad (1)$$

$$(n = 15; r^2 = 0.96; s = 127.66; F = 301.92; q^2 = 0.94; S_{PRESS} = 1.463; \text{outlier: C15})$$

where n is the number of data points and s is the standard deviation. The outliers were identified by BuildQSAR software [41] and were then removed if: $|Y_{\text{obs}} - Y_{\text{calc}}| \geq 2 \times \text{standard deviation}$.

Table 4. The descriptor values of molar refractivity (MR), molecular volume (MV), polarizability (POLZ), superficial tension (ST), and ¹³C nuclear magnetic resonance (NMR) shift chemical (δ_{C1} and δ_{C2}) for each corrole (C1–C17).



Compound	MR	MV	POLZ	ST	δ_{C1}	δ_{C2}
C1	90.28	214.0	35.8	78.2	83.0	136.3
C2	164.0	409.8	65.0	63.4	105.1	135.0
C3	164.0	422.5	65.0	60.4	105.1	139.3
C4	164.0	422.5	65.0	60.4	105.1	135.0
C5	164.0	422.5	65.0	60.4	101.8	131.5
C6	164.0	435.1	65.0	57.7	105.1	139.3
C7	164.0	435.1	65.0	57.7	101.8	135.8

Table 4. Cont.

Compound	MR	MV	POLZ	ST	δ_{C1}	δ_{C2}
C8	164.0	435.1	65.0	57.7	105.1	139.3
C9	164.0	435.1	65.0	57.7	105.1	143.6
C10	164.0	435.1	65.0	57.7	101.8	131.5
C11	164.0	435.1	65.0	57.7	105.1	135.0
C12	164.0	447.7	65.0	55.2	101.8	135.8
C13	164.0	447.7	65.0	55.2	101.8	131.5
C14	164.0	460.3	65.0	53.0	101.8	135.8
C15	164.0	460.3	65.0	53.0	101.1	143.6
C16	164.0	460.3	65.0	53.0	101.8	135.8
C17	164.0	473.0	65.0	51.0	101.8	140.1

3. Discussion

The molecular docking technique has become one of the most used methods for determining the drug targets, offering an atomic-level explanation on the binding capacity for screening potential compounds for future in vitro assays [44–46]. This approach has been widely explored for repurposing clinically approved drugs, natural products, or novel synthetic compounds as potential candidates to inhibit SARS-CoV-2 replication via the inhibition of viral proteases [10–16,44]. Thus, in silico calculations via molecular docking was applied to suggest the interaction mechanism of 17 potential synthetic corrole derivatives (C_6H_5 -corrole) into both M^{Pro} and PL^{Pro} proteins of SARS-CoV-2. Additionally, the fluorine effect on C_6H_5 -corrole structure was also evaluated in terms of binding affinity and 2D-QSAR correlations. The tested compounds will pave the way for the development/design of drugs to inhibit SARS-CoV-2.

The M^{Pro} structure is a dimer, and each monomer is divided into three different domains: domains I (8–100 residues), II (101–183 residues), and III (200–303 residues) presenting the amino acid residues His-41 and Cys-145 (catalytic dyad) in the domains I and II, respectively (catalytic site is not close to the dimer interface). The substrate-binding site is positioned inside a cleft (pockets S1, S1', S2, and S4) between domains I and II [44,47]. It has been reported that the imidazole from His-41 residue makes a strong hydrogen bond with a water molecule (previously namely as H_2O_{cat}), suggesting that this water may play a role as a third catalytic residue, completing the noncanonical catalytic triad in M^{Pro} [48–50] (Figure 2A). Thus, all molecular docking calculations were carried out considering the presence of H_2O_{cat} into the catalytic pocket in the position corresponding to the crystallographic structure of M^{Pro} [51].

In this case, the addition of phenyl rings in the *meso* positions (corresponding to the carbons 5, 10, and 15) of the corrole core significantly increased the docking score value, from 25.76 to 35.68 dimensionless for C1 and C2, respectively, indicating that the increase of the ligand area through phenyl moieties did not negatively impact the binding capacity (theoretical area of 306.19 and 544.98 Å² for C1 and C2, respectively) being able to be accommodated inside the protein pocket, without a hindrance, and increase the connecting points. The insertion and position of fluorine atoms into the phenyl moiety (C3–C17) directly impacted the binding capacity of C_6H_5 -corrole, as an example the docking score value for the mono-substituted-fluorinated-corroles C3–C5 decreased drastically for the fluorine atom in the *para* position, suggesting a possible electrostatic dependence. The total analysis of the docking score value for all fluorinated-corroles to M^{Pro} clearly suggested that independently of the number of fluorine atoms in the phenyl ring, at least one fluorine atom in the *para* position decreased the docking score value, showing a quite similar value compared with C1 (Table 1), reinforcing the possible electrostatic dependence. On the other hand, all the fluorinated-corroles without a fluorine atom in the *para* position increased the binding affinity of the corroles to M^{Pro} (Table 1). In this sense, when analyzing the same group corresponding to the number of fluorine atoms in the phenyl moiety, the ligands

presented different poses (there is not a clear superposition), which is mainly impacted with fluorine atoms in the *para* position.

Van der Waals interactions and hydrogen bonding corroborate with the binding capacity of M^{Pro} :C1–C17, however, hydrogen bonding was not detected in C2. There is a connect point dependence for the ranking of the binding affinity of the corroles to M^{Pro} ; as an example, the corrole C1 which presented a lower docking score value than C2, showed a total of five connected points (Met-49, Asn-142, Cys-145, Met-165, and Gln-189 residues), while C2 showed seven connected points (Leu-27, His-41, Met-49, Cys-145, Met-165, Pro-168, and Gln-189 residues). The same trend was also observed for all the fluorinated compounds comparing di- (C6–C11), tri- (C12, C13), or tetra- (C14–C16) fluorinated-corroles with the fluorine atoms in the *para* position with those in the *ortho* and/or *meta* position into the phenyl moieties. As an example, the di-fluorinated-corroles with fluorine atoms in the *para* position (C7 and C10) presented five connected points (Leu-27, His-41, Met-49, Asn-142, Gln-189 residues), while the di-fluorinated-corroles with fluorine atoms in the *ortho/meta* positions (C6, C8, C9, and C11) presented ten connected points (Thr-25, Leu-27, His-41, Met-49, Asn-142, Gly-143, Cys-145, Met-165, Leu-167, and Gln-189 residues). Differently for the cited fluorinated-corroles, the mono-fluorinated-corroles did not show a connected point dependence, but there is a significant difference in the docking pose compared to compounds C3/C4 with C5, suggesting that the binding capacity of the studied mono-fluorinated-corroles is closely dependent on the arrangement (buried or not) inside the protein cavity.

The molecular docking calculations also suggested that the good binding affinity of C2 and *ortho/meta*-fluorinated-corroles is also dependent on the capacity to interact with the two amino acid residues that are responsible for the catalytic dyad (His-41 and Cys-145), while C1 and *para*-fluorinated-corroles presented an interaction with just one amino acid residue of the catalytic dyad, e.g., the compounds C3 and C4 interacted with His-41 and Cys-145 residues via van der Waals forces within a distance of 2.70 and 3.00 Å, respectively, while the compound C5 only interacted with Cys-145 residue within a distance of 3.70 Å (Table 2).

Differently from the M^{Pro} enzyme, the PL^{Pro} is a trimer that is composed of chains A, B, and C whose activity is related to the triad catalytic amino acid residues that are composed of Cys-112, His-273, and Asp-287, without the contribution of a H_2O_{cat} [52]. Molecular docking results suggested that the presence of phenyl moieties in the corrole structure positively impacted the binding capacity of this corrole, improving the docking score value of seven punctuation, probably not due to the increase of connecting points but due to the proximity of the ligand structure with the amino acid residues of the protease (Table 3). The fluorine atoms in the phenyl moieties also impacted the binding capacity of *meso*-aryl-corroles to PL^{Pro} . In this case, opposing the results that were obtained for M^{Pro} compared to the docking score values for fluorinated-corroles to PL^{Pro} , there is not any trend based on the fluorine position, specifically in the *para* position (R_3). However, a feasible trend can be noticed based on the insertion at least tri-fluorine atoms into phenyl moieties that increased the docking score value and fitted better into the PL^{Pro} catalytic pocket.

For PL^{Pro} , molecular docking calculations suggested van der Waals as the main intermolecular forces that are responsible for the complex stabilization, however, hydrogen bonding was also detected, except for C1, C2, and C5. In the present model for PL^{Pro} :C1–C17 was not detected with a specific trend based on connecting points and hydrogen bonding as previously described for M^{Pro} .

The calculated ligand affinity to its target significantly depends on the charge states of the residues in the binding pocket and even the ligand [53]. Therefore, it is important to highlight that the GOLD 2020.2 software that was used in this work for molecular docking added hydrogen atoms to the proteases following tautomeric states and ionization data at a physiological pH (pH = 7.4). Since the evaluated corroles theoretically interact with the catalytic site of the proteases which harbors the catalytic amino acid residues His-41 and Cys-145 in M^{Pro} and Cys-112, His-273, and Asp-287 in PL^{Pro} , from a mechanistic point of

view, the amino acid residue Cys should be a nucleophile while His is similar to a general acid that there is the assistance of the negatively charged Asp in the case of PL^{PRO} [54]. Thus, in this work, Cys and His are in the neutral form which are less likely to be stable in vitro or in vivo from a mechanistic way (Cys should have a significantly downshifted pK_a so that it is charged, while the His should have a high pK_a to stay charged) [55].

The 2D-QSAR models obtained a correlation of the docking score values for M^{PRO}, while for PL^{PRO} there is not a clear correlation. In fact, no 2D-QSAR model was obtained using MR, MV, and POLZ descriptors and they were not useful. However, it was shown that δ_{C-1} was present as a descriptor in the 2D-model, because without it there would be no proposition of the model. For M^{PRO}:C1–C17, a sigmoidal correlation between the docking score values and dual electronic parameters (σ_I and σ_R) was obtained, indicating two separated regions of higher and lower affinity. In this case the lower affinity and score values were observed for the corroles with a fluorine atom in the *para* position (R₃). From the correlation between the docking score value of M^{PRO}:C2–C17 and ¹³C NMR chemical shifts of the sp² carbons atoms (δ_{C-1} and δ_{C-2}) that were adjacent to the fluorinated ring a favored mathematical model by downfield of the δ_{C-1} was observed, reinforcing that the interaction between M^{PRO} and C₆H₅-corroles might be increasing due to the decrease in the electronic density of the C₆H₅-corrole core. Since hydrogen bonding (HB) is strongly affected by electronic density, probably these effects can be due to HB interactions. Moreover, the 2D-model indicated an independent variable that contributes more to the model, probably due to the van der Waals interactions which were previously described in the molecular docking as the main intermolecular forces for the interaction between the studied corroles with M^{PRO}. The obtained 2D-QSAR model might be improved by the incorporation of experimental data, even from the literature using the same organic class that was assayed in this work, however, there are few reports on the application of tetrapyrrolic macrocycles (porphyrinoid molecules) to inhibit SARS-CoV-2 and these reports only focus on spike protein interactions which is not the target of this work [56–58].

4. Materials and Methods

4.1. In Silico Calculations Procedure

The three-dimensional structure of the SARS-CoV-2 proteases PL^{PRO} and M^{PRO} was obtained from the Protein Data Bank with access code 6W9C and 6LU7, respectively [51,52]. Spartan'18 software (Wavefunction, Inc., Irvine, CA, USA) [59] was used to build the three-dimensional structure of the corroles C1–C17. The same software optimized the chemical structure of the ligands by Density Functional Theory (DFT) approximation. GOLD 2020.2 software (Cambridge Crystallographic Data Center Software Ltd., Cambridge, UK) [60] was used to add hydrogen atoms to the structure of the proteases according to ionization at pH 7.4 and tautomeric states were inferred by the software. The same software was used for molecular docking calculations defining an 8 Å radius around the active binding site of each enzyme. The scoring function ASP was used in the docking calculations due to the lowest root mean square deviation (RMSD) that was obtained via redocking studies. PyMOL Delano Scientific LLC software (DeLano Scientific LLC: San Carlos, CA, USA) [61] was used to identify the main amino acid residues that interact with the ligands and to build the final representation.

4.2. The 2D-QSAR Procedure

Molecular descriptors for each *meso*-aryl-corrole (C2–C17) were drawn by ACD/ChemSketch 4.0 software (ACDLabs software package, version 12.0, Toronto, ON, Canada) [40]. The physico-chemical properties were predicted by this software using additive atomic or group increments (depending on the bonds, e.g., single, double, and aromatic of an atom and on its neighboring atoms). The ACD/ChemSketch algorithm is composed of basic and derived macroscopic properties using a large experimental database relating structure to density, refractive index, and surface tension [62].

The following parameters were obtained: polarizability (POLZ), superficial tension (ST), molar volume (MV), molar refractivity (MR), and the ^{13}C nuclear magnetic resonance (NMR) chemical shifts of the sp^2 carbons atoms ($\delta_{\text{C-1}}$ and $\delta_{\text{C-2}}$) adjacent to the phenyl moiety containing fluorine atoms. The 2D-QSAR data was carried out by multiple regression analyses. All these correlations were performed by the BuildQSAR 1.0 software (Universidade Federal do Espírito Santo, Vitória, Espírito Santo, Brazil) [41]. The best descriptors were obtained by genetic algorithm, and the 2D-QSAR model was processed in terms of the highest correlation coefficient or F -test equations, and the lowest standard deviation equations following literature [40]. The correlation equations were obtained along with the statistical parameters, as n is the number of data points, r is the correlation coefficient, s is the standard deviation, q^2 is the cross validation, S_{PRESS} is the standard deviation of the cross validation (q^2 and S_{PRESS} are the cross-correlation), and F is Fisher value measure for the statistical significance. In the equations of this work, the numbers in parentheses represent the 95% confidence intervals of the coefficients [40,41,43,63]. Also, the correlations with the score values that were obtained from molecular docking for M^{Pro} and PL^{Pro} with electronic parameters [64] (Hammett constants, dual parameters, and Swain–Lupton inductive and resonance parameters) and lipophilic parameter ($\log P$, [65]) were performed using the Origin 6.0 software (OriginLab Corporation, Northampton, MA, USA).

5. Conclusions

Molecular docking calculations indicated that the addition of phenyl rings in the *meso* positions of the corrole core positively impacted the interaction with both proteases of SARS-CoV-2, increasing the docking score value. The insertion and position of fluorine atoms into the phenyl moieties directly impacted the binding capacity of C_6H_5 -corrole. In the case for M^{Pro} , independently of the number of fluorine atoms in the phenyl rings, at least one fluorine atom in the *para* position decreases the docking score value, negatively impacting the interaction with this protease. Moreover, the 2D-QSAR model for M^{Pro} :**C1–C17** showed a sigmoidal correlation between the docking score values and dual electronic parameters (σ_{I} and σ_{R}), indicating two separated regions of higher and lower affinity, as well as was obtained one mathematical model correlating docking score values (M^{Pro} :**C2–C17**) and the ^{13}C NMR chemical shifts of the sp^2 carbons atoms ($\delta_{\text{C-1}}$ and $\delta_{\text{C-2}}$) adjacent to the fluorinated ring, corroborating with the molecular docking trend. On the other hand, the molecular docking results for PL^{Pro} indicated that the binding capacity into the PL^{Pro} catalytic pocket increased with the insertion of tri- or more fluorine-atoms into phenyl moieties. Overall, corrole and *meso*-aryl-corrole might interact indiscriminately in the M^{Pro} or PL^{Pro} catalytic site, while the fluorinated-corroles which do not present *para*-fluorine atoms (**C2**, **C3**, **C4**, **C6**, **C8**, **C9**, **C15**, and **C11**) might interact preferentially in the M^{Pro} catalytic site. Despite the results being only based on a molecular modeling approach (one initial step to identify potential drugs), we consider the evaluated fluorinated corroles as potential compounds for future experimental assays in inhibiting SARS-CoV-2 replication by targeting viral proteases, mainly M^{Pro} .

Author Contributions: Conceptualization, O.A.C.; methodology, O.A.C.; software, O.A.C., C.E.R.-S., and Á.E.; validation, formal analysis, and data curation, O.A.C., C.Q.S., N.F.-R., J.R.T., C.E.R.-S., and Á.E.; supervision, H.C.C.-F.-N. and T.M.L.e.S.; resources, H.C.C.-F.-N. and T.M.L.e.S.; project administration, H.C.C.-F.-N. and T.M.L.e.S.; writing—original draft preparation, O.A.C., C.E.R.-S., and Á.E.; writing—review and editing, O.A.C., H.C.C.-F.-N., and T.M.L.e.S.; funding acquisition, H.C.C.-F.-N. and T.M.L.e.S. All authors have read and agreed to the published version of the manuscript.

Funding: This research was funded by the Brazilian agencies Conselho Nacional de Desenvolvimento Científico e Tecnológico (CNPq, Finance Codes 441019/2020-0, 307162/2017-6) and Fundação de Amparo à Pesquisa do Estado do Rio de Janeiro (FAPERJ, Finance Codes E-26/210.182/2020, E-26/201.067/2021, E-26/210.112/2020). This study was financed in part by Coordenação de Aperfeiçoamento de Pessoal de Nível Superior (CAPES, Brazil, Finance Code 88887.506989/2020-00). Funding was also provided by CNPq, CAPES, and FAPERJ through the National Institutes of Sci-

ence and Technology Program (INCT) on Diseases of Neglected Populations (INCT-IDPN, Finance Code 465313/2014-0).

Institutional Review Board Statement: Not applicable.

Informed Consent Statement: Not applicable.

Data Availability Statement: The data presented in this study are all available in the article. Raw data are available from the authors upon request.

Acknowledgments: O.A.C. thanks Dumith Chequer Bou-Habib and Fundação para o Desenvolvimento Científico e Tecnológico em Saúde (FIOTEC), both from the Oswaldo Cruz Foundation, for the grant VPPCB-005-FIO-20. C.E.R.-S. and A.E. also thank Anderson Coser Gaudio (Universidade Federal do Espírito Santo, Vitória, Brazil) for the freeware use of the BuildQSAR 1.0 software.

Conflicts of Interest: The authors declare no conflict of interest. Additionally, the funders had no role in the design of the study; in the collection, analyses, or interpretation of data; in the writing of the manuscript; or in the decision to publish the results.

Abbreviations

Chymotrypsin-like cysteine protease (3CL^{Pro}), main protease (M^{Pro}), papain-like protease (PL^{Pro}), severe acute respiratory syndrome coronavirus 2 (SARS-CoV-2), Middle East respiratory syndrome (MERS), 2019 coronavirus disease (COVID-19), two-dimensional quantitative structure–activity relationship (2D-QSAR), World Health Organization (WHO), ribonucleic acid (RNA), U.S. Food and Drug Administration (FDA), variants of concern (VoC), open reading frame (ORF), polarizability (POLZ), superficial tension (ST), lipophilicity (logP), molar volume (MV), molar refractivity (MR), nuclear magnetic resonance (NMR), correlation coefficient (r^2), Fisher (F), cross validated (q^2), and standard deviation of cross validation (S_{PRESS}).

References

1. Dos Santos, W.G. Natural history of COVID-19 and current knowledge on treatment therapeutic options. *Biomed. Pharmacother.* **2020**, *129*, 110493. [CrossRef] [PubMed]
2. COVID-19 Dashboard by the Center for Systems Science and Engineering (CSSE) at Johns Hopkins University (JHU). Available online: <https://coronavirus.jhu.edu/map.html> (accessed on 28 August 2022).
3. Liu, X.-H.; Zhang, X.; Lu, Z.-H.; Zhu, Y.-S.; Wang, T. Potential molecular targets of nonstructural proteins for the development of antiviral drugs against SARS-CoV-2 infection. *Biomed. Pharmacother.* **2021**, *133*, 111035. [CrossRef] [PubMed]
4. Chaves, O.A.; Fintelman-Rodrigues, N.; Wang, X.; Sacramento, C.Q.; Temerozo, J.R.; Ferreira, A.C.; Mattos, M.; Pereira-Dutra, F.; Bozza, P.T.; Castro-Faria-Neto, H.C.; et al. Commercially Available Flavonols Are Better SARS-CoV-2 Inhibitors than Isoflavone and Flavones. *Viruses* **2022**, *14*, 1458. [CrossRef]
5. Ali, F.; Kasry, A.; Amin, M. The new SARS-CoV-2 strain shows a stronger binding affinity to ACE2 due to N501Y mutant. *Med. Drug Discov.* **2021**, *10*, 100086. [CrossRef]
6. Dalmat, Y.-M. SARS-CoV-2 histoire de mutants. *Option/Bio* **2021**, *32*, 10. [CrossRef]
7. Sharma, T.; Abohashrh, M.; Baig, M.H.; Dong, J.-J.; Alam, M.M.; Ahmad, I.; Irfan, S. Screening of drug databank against WT and mutant main protease of SARS-CoV-2: Towards finding potential compound for repurposing against COVID-19. *Saudi J. Biol. Sci.* **2021**, *28*, 3152–3159. [CrossRef] [PubMed]
8. Coronavirus (COVID-19) | Drugs. Available online: <https://www.fda.gov/drugs/emergency-preparedness-drugs/coronaviruscovid-19-drugs> (accessed on 15 August 2022).
9. Beigel, J.H.; Tomashek, K.M.; Dodd, L.E.; Mehta, A.K.; Zingman, B.S.; Kalil, A.C.; Hohmann, E.; Chu, H.Y.; Luetkemeyer, A.; Kline, S.; et al. Remdesivir for the treatment of COVID-19-Final report. *N. Engl. J. Med.* **2020**, *383*, 1813–1826. [CrossRef] [PubMed]
10. Rangsinth, P.; Sillapachaiyaporn, C.; Nilkhet, S.; Tencomnao, T.; Ung, A.T.; Chuchawankul, S. Mushroom-derived bioactive compounds potentially serve as the inhibitors of SARS-CoV-2 main protease: An in silico approach. *J. Tradit. Complement. Med.* **2021**, *11*, 158–172. [CrossRef]
11. Banerjee, R.; Perera, L.; Tillekeratne, L.M.V. Potential SARS-CoV-2 main protease inhibitors. *Drug Discov. Today* **2021**, *26*, 804–816. [CrossRef]
12. Fintelman-Rodrigues, N.; Sacramento, C.Q.; Lima, C.R.; da Silva, F.S.; Ferreira, A.C.; Mattos, M.; de Freitas, C.S.; Soares, V.C.; Dias, S.S.G.; Temerozo, J.R.; et al. Atazanavir, alone or in combination with ritonavir, inhibits SARS-CoV-2 replication and proinflammatory cytokine production. *Antimicrob. Agents Chemother.* **2020**, *64*, e00825-20. [CrossRef]
13. Anand, K.; Ziebuhr, J.; Wadhwani, P.; Mesters, J.R.; Hilgenfeld, R. Coronavirus main proteinase (3CL^{Pro}) structure: Basis for design of anti-SARS drugs. *Science* **2003**, *300*, 1763–1767. [CrossRef] [PubMed]

14. Chaves, O.A.; Sacramento, C.Q.; Ferreira, A.C.; Mattos, M.; Fintelman-Rodrigues, N.; Temerozo, J.R.; Vazquez, L.; Pinto, D.P.; Silveira, G.P.E.; Fonseca, L.B.; et al. Atazanavir is a competitive inhibitor of SARS-CoV-2 Mpro, impairing variants replication in vitro and in vivo. *Pharmaceuticals* **2022**, *15*, 21. [CrossRef] [PubMed]
15. Chaves, O.A.; Sacramento, C.Q.; Fintelman-Rodrigues, N.; Temerozo, J.R.; Pereira-Dutra, F.; Mizurini, D.M.; Monteiro, R.Q.; Vazquez, L.; Bozza, P.T.; Castro-Faria-Neto, H.C.; et al. Apixaban, an orally available anticoagulant, inhibits SARS-CoV-2 replication and its major protease in a non-competitive way. *J. Mol. Cell Biol.* **2022**, *6*, mjac039. [CrossRef] [PubMed]
16. Santos-Filho, O.A. Identification of potential inhibitors of severe acute respiratory syndrome-related coronavirus 2 (SARS-CoV-2) main protease from non-natural and natural sources: A molecular docking study. *J. Braz. Chem. Soc.* **2020**, *31*, 2638–2643. [CrossRef]
17. Báez-Santos, Y.M.; St. John, S.E.; Mesecar, A.D. The SARS coronavirus papain-like protease: Structure, function and inhibition by designed antiviral compounds. *Antivir. Res.* **2015**, *115*, 21–38. [CrossRef]
18. Rajpoot, S.; Alagumuthu, M.; Baig, M.S. Dual targeting of 3CLpro and PLpro of SARS-CoV-2: A novel structure-base design approach to treat COVID-19. *Curr. Res. Struct. Biol.* **2021**, *3*, 9–18. [CrossRef]
19. Bzówka, M.; Mitusińska, K.; Raczyńska, A.; Samol, A.; Tuszyński, J.A.; Góra, A. Structural and evolutionary analysis indicate that the SARS-CoV-2 Mpro is a challenging target for small-molecule inhibitor design. *Int. J. Mol. Sci.* **2020**, *21*, 3099. [CrossRef]
20. Lv, Z.; Cano, K.E.; Jia, L.; Drag, M.; Huang, T.T.; Olsen, S.K. Targeting SARS-CoV-2 proteases for COVID-19 antiviral development. *Front. Chem.* **2022**, *9*, 819165. [CrossRef]
21. Amin, S.A.; Banerjee, S.; Ghosh, K.; Gayen, S.; Jha, T. Protease targeted COVID-19 drug discovery and its challenges: Insight into viral main protease (Mpro) and papain-like protease (PLpro) inhibitors. *Bioorg. Med. Chem.* **2021**, *29*, 115860. [CrossRef]
22. Pfizer's Novel COVID-19 Oral Antiviral Treatment Candidate Reduced Risk of Hospitalization or Death by 89% in Interim Analysis of Phase 2/3 Epic-HR Study. Available online: <https://www.pfizer.com/news/press-release/press-release-detail/pfizers-novel-covid-19-oral-antiviral-treatment-candidate> (accessed on 15 August 2022).
23. Ahmad, B.; Batool, M.; Ain, Q.U.; Kim, M.S.; Choi, S. Exploring the binding mechanism of PF-07321332 SARS-CoV-2 protease inhibitor through molecular dynamics and binding free energy simulations. *Int. J. Mol. Sci.* **2021**, *22*, 9124. [CrossRef]
24. Acunha, T.V.; Chaves, O.A.; Iglesias, B.A. Fluorescent pyrene moiety in fluorinated C₆F₅-corroles increases the interaction with HSA and CT-DNA. *J. Porphyr. Phthalocyanines* **2021**, *25*, 75–94. [CrossRef]
25. Ding, T.; Alemán, E.A.; Modarelli, D.A.; Ziegler, C.J. Photophysical properties of a series of free-base corroles. *J. Phys. Chem. A* **2005**, *109*, 7411–7417. [CrossRef] [PubMed]
26. Ventura, B.; Esposti, A.D.; Koszarna, B.; Gryko, D.T.; Flamigni, L. Photophysical characterization of free-base corroles, promising chromophores for light energy conversion and singlet oxygen generation. *New J. Chem.* **2005**, *29*, 1559–1566. [CrossRef]
27. Acunha, T.V.; Matiuzzi, B.R.; Silva, J.A.; Galindo, D.D.M.; Chaves, O.A.; Rocha, V.N.; Piquini, P.C.; Kohler, M.H.; Boni, L.; Iglesias, B.A. Unveiling the photophysical, biomolecule binding and photo-oxidative capacity of novel Ru(II)-polypyridyl corroles: A multipronged approach. *J. Mol. Liq.* **2021**, *340*, 117223. [CrossRef]
28. Zhang, Z.; Yu, H.-J.; Huang, H.; Wang, H.-H.; Wu, S.; Liu, H.-Y.; Zhang, H.-T. The photodynamic activity and toxicity evaluation of 5,10,15-tris(ethoxycarbonyl)corrole phosphorus(V) in vivo and in vitro. *Eur. J. Med. Chem.* **2019**, *163*, 779–786. [CrossRef]
29. Bornhuetter, T.; Shamali, N.; Saltsman, I.; Mahammed, A.; Gross, Z.; Daeschlein, G.; Roeder, B. Singlet oxygen luminescence kinetics under PDI relevant conditions of pathogenic dermatophytes and molds. *J. Photochem. Photobiol. B* **2018**, *178*, 606–613. [CrossRef]
30. Goslinska, T.; Piskorz, J. Fluorinated porphyrinoids and their biomedical applications. *J. Photochem. Photobiol. C* **2011**, *12*, 304–321. [CrossRef]
31. Teo, R.D.; Hwang, J.Y.; Termini, J.; Gross, Z.; Gray, H.B. Fighting cancer with corroles. *Chem. Rev.* **2017**, *117*, 2711–2729. [CrossRef]
32. Aviezer, D.; Cotton, S.; David, M.; Segev, A.; Khaselev, N.; Galili, N.; Gross, Z.; Yayon, A. Porphyrin analogues as novel antagonists of fibroblast growth factor and vascular endothelial growth factor receptor binding that inhibit endothelial cell proliferation, tumor progression, and metastasis. *Cancer Res.* **2000**, *60*, 2973–2980.
33. Romeo, A.; Iacovelli, F.; Falconi, M. Targeting the SARS-CoV-2 spike glycoprotein prefusion conformation: Virtual screening and molecular dynamics simulations applied to the identification of potential fusion inhibitors. *Virus Res.* **2020**, *286*, 198068. [CrossRef]
34. Gu, C.; Wu, Y.; Guo, H.; Zhu, Y.; Xu, W.; Wang, Y.; Zhou, Y.; Sun, Z.; Cai, X.; Li, Y.; et al. Protoporphyrin IX and verteporfin potently inhibit SARS-CoV-2 infection in vitro and in a mouse model expressing human ACE2. *Sci. Bull.* **2021**, *66*, 925–936. [CrossRef] [PubMed]
35. Kipshidze, N.; Yeo, N.; Kipshidze, N. Photodynamic therapy for COVID-19. *Nat. Photonics* **2020**, *14*, 651–652. [CrossRef]
36. Conrado, P.C.V.; Sakita, K.M.; Arita, G.S.; Galinari, C.B.; Gonçalves, R.S.; Lopes, L.D.G.; Lonardoni, M.V.C.; Teixeira, J.J.V.; Bonfim-Mendonça, P.S.; Kioshima, E.S. A systematic review of photodynamic therapy as an antiviral treatment: Potential guidance for dealing with SARS-CoV-2. *Photodiagnosis Photodyn. Ther.* **2021**, *34*, 102221. [CrossRef]
37. Shah, P.; Westwell, A.D. The role of fluorine in medicinal chemistry. *J. Enzym. Inhib. Med. Chem.* **2007**, *22*, 527–540. [CrossRef] [PubMed]
38. Chaves, O.A.; Barros, L.S.; Oliveira, M.C.C.; Sant'Anna, C.M.R.; Ferreira, A.B.B.; Silva, F.A.; Cesarin-Sobrinho, D.; Netto-Ferreira, J.C. Biological interactions of fluorinated chalcones: Stimulation of tyrosinase activity and binding to bovine serum albumin. *J. Fluor. Chem.* **2017**, *199*, 30–38. [CrossRef]

39. Chaves, O.A.; Oliveira, C.H.C.S.; Ferreira, R.C.; Melos, J.L.R.; Rodrigues-Santos, C.E.; Echevarria, A.; Cesarin-Sobrinho, D. Investigation of interaction between human plasmatic albumin and potential fluorinated anti-trypanosomal drugs. *J. Fluor. Chem.* **2017**, *199*, 103–112. [CrossRef]
40. Spessard, G.O. ACD Labs/LogP dB 3.5 and ChemSketch 3.5. *J. Chem. Inf. Comput. Sci.* **1998**, *19*, 1250–1253. [CrossRef]
41. de Oliveira, D.B.; Gaudio, A.C. BuildQSAR: A new computer program for QSAR analysis. *Mol. Inform.* **2001**, *19*, 599–601. [CrossRef]
42. Eriksson, L.; Jaworska, J.; Worth, A.P.; Cronin, M.T.; McDowell, R.M.; Gramatica, P. Methods for reliability and uncertainty assessment and for applicability evaluations of classification- and regression-based QSARs. *Environ. Health Perspect.* **2003**, *111*, 1361–1375. [CrossRef]
43. Gaudio, A.C.; Zandonade, E. Proposição, validação e análise dos modelos que correlacionam estrutura química e atividade biológica. *Quim. Nova* **2001**, *24*, 658–671. [CrossRef]
44. Muhammad, I.A.; Muangchoo, K.; Muhammad, A.; Ajingi, Y.S.; Muhammad, I.Y.; Umar, I.D.; Muhammad, A.B. A Computational study to identify potential inhibitors of SARS-CoV-2 main protease (Mpro) from Eucalyptus active compounds. *Computation* **2020**, *8*, 79. [CrossRef]
45. Debia, N.P.; Rodríguez, J.J.P.; da Silveira, C.H.; Chaves, O.A.; Iglesias, B.A.; Rodembusch, F.S.; Lüdtke, D.S. Synthesis and photophysics of benzazole based triazoles with amino acid-derived pendant units. Multiparametric optical sensors for BSA and CT-DNA in solution. *J. Mol. Liq.* **2020**, *309*, 113092. [CrossRef]
46. Bombaça, A.C.S.; Silva, L.A.; Chaves, O.A.; da Silva, L.S.; Barbosa, J.M.C.; da Silva, A.M.; Ferreira, A.B.B.; Menna-Barreto, R.F.S. Novel N,N-di-alkylnaphthoimidazolium derivative of β -lapachone impaired *Trypanosoma cruzi* mitochondrial electron transport system. *Biomed. Pharmacother.* **2021**, *135*, 111186. [CrossRef]
47. Tahir ul Qamar, M.; Alqahtani, S.M.; Alamri, M.A.; Chen, L.-L. Structural basis of SARS-CoV-2 3CL pro and anti-COVID-19 drug discovery from medicinal plants. *J. Pharm. Anal.* **2020**, *10*, 313–319. [CrossRef] [PubMed]
48. Kneller, D.W.; Phillips, G.; O'Neill, H.M.; Jedrzejczak, R.; Stols, L.; Langan, P.; Joachimiak, A.; Coates, L.; Kovalevsky, A. Structural plasticity of SARS-CoV-2 3CL Mpro active site cavity revealed by room temperature X-ray crystallography. *Nat. Comm.* **2020**, *11*, 3202. [CrossRef] [PubMed]
49. Lee, J.; Worrall, L.J.; Vuckovic, M.; Rosell, F.I.; Gentile, F.; Ton, A.-T.; Caveney, N.A.; Ban, F.; Cherkasov, A.; Paetzel, M.; et al. Crystallographic structure of wild-type SARS-CoV-2 main protease acyl-enzyme intermediate with physiological C-terminal autoprocessing site. *Nat. Commun.* **2020**, *11*, 5877. [CrossRef] [PubMed]
50. Ramos-Guzman, C.A.; Ruiz-Pernía, J.J.; Tuñon, I. Unraveling the SARS-CoV-2 main protease mechanism using multiscale methods. *ACS Catal.* **2020**, *21*, 12544–12554. [CrossRef]
51. Osipiuk, J.; Azizi, S.-A.; Dvorkin, S.; Endres, M.; Jedrzejczak, R.; Jones, K.A.; Kang, S.; Kathayat, R.S.; Kim, Y.; Lisnyak, V.G.; et al. Structure of papain-like protease from SARS-CoV-2 and its complexes with non-covalent inhibitors. *Nat. Commun.* **2021**, *12*, 743. [CrossRef]
52. Gao, X.; Qin, B.; Chen, P.; Zhu, K.; Hou, P.; Wojdyla, J.A.; Wang, M.; Cui, S. Crystal structure of SARS-CoV-2 papain-like protease. *Acta Pharm. Sin. B* **2021**, *11*, 237–245. [CrossRef]
53. Harris, R.C.; Tsai, C.-C.; Ellis, C.R.; Shen, J. Proton-coupled conformational allostery modulates the inhibitor selectivity for β -secretase. *J. Phys. Chem. Lett.* **2017**, *8*, 4832–4837. [CrossRef]
54. Barretto, N.; Jukneliene, D.; Ratia, K.; Chen, Z.; Mesecar, A.D.; Baker, S.C. The papain-like protease of severe acute respiratory syndrome coronavirus has deubiquitinating activity. *J. Virol.* **2005**, *79*, 15189–15198. [CrossRef] [PubMed]
55. Henderson, J.A.; Verma, N.; Harris, R.C.; Liu, R.; Shen, J. Assessment of proton-coupled conformational dynamics of SARS and MERS coronavirus papain-like proteases: Implication for designing broad-spectrum antiviral inhibitors. *J. Chem. Phys.* **2020**, *153*, 115101. [CrossRef]
56. Lechuga, G.C.; Souza-Silva, F.; Sacramento, C.Q.; Trugilho, M.R.O.; Valente, R.H.; Napoleão-Pêgo, P.; Dias, S.S.G.; Fintelman-Rodrigues, N.; Temerozo, J.R.; Carels, N.; et al. SARS-CoV-2 proteins bind to hemoglobin and its metabolites. *Int. J. Mol. Sci.* **2021**, *22*, 9035. [CrossRef]
57. Gubarev, Y.A.; Lebedeva, N.S.; Yurina, E.S.; Syrbu, S.S.; Kiselev, A.N.; Lebedev, M.A. Possible therapeutic targets and promising drugs based on unsymmetrical hetaryl-substituted porphyrins to combat SARS-CoV-2. *J. Pharm. Anal.* **2021**, *11*, 691–698. [CrossRef]
58. Koifman, O.I.; Lebedeva, N.S.; Gubarev, Y.A.; Koifman, M.O. Modeling the binding of protoporphyrin IX, verteporfin, and chlorin e6 to SARS-CoV-2 proteins. *Chem. Heterocycl. Compd.* **2021**, *57*, 423–431. [CrossRef] [PubMed]
59. Wavefunction-Chemistry at Your Fingertips. Available online: <https://www.wavefun.com/> (accessed on 15 August 2022).
60. Cambridge Crystallographic Data Center. Available online: <http://www.ccdc.cam.ac.uk/solutions/csd-discovery/components/gold/> (accessed on 15 August 2022).
61. PyMol Delano. Available online: <https://pymol.org/2/> (accessed on 15 August 2022).
62. Osterberg, T.; Norinder, U. Prediction of drug transport processes using simple parameters and PLS statistics. The use of ACD/logP and ACD/ChemSketch descriptors. *Eur. J. Pharm. Sci.* **2001**, *12*, 327–337. [CrossRef]
63. Rodrigues-Santos, C.E.; Leonor, L.; Bortoluzzi, A.J.; Canto-Cavalheiro, M.M.; Machado, G.C.; Echevarria, A. Synthesis, antileishmanial activity and structure–activity relationship of 1-N-X-phenyl-3-N'-Y-phenyl-benzamidines. *Eur. J. Med. Chem.* **2013**, *67*, 166–174. [CrossRef] [PubMed]

64. Isaacs, N.S. *Physical Organic Chemistry*, 2nd ed.; Prentice Hall: Hoboken, NJ, USA, 1995.
65. SwissADEME. Available online: www.swissademe.ch (accessed on 15 August 2022).